

Cite this: *J. Mater. Chem. A*, 2017, 5, 13950Received 19th April 2017
Accepted 24th May 2017

DOI: 10.1039/c7ta03392c

rsc.li/materials-a

Robust $\text{LiTi}_2(\text{PO}_4)_3$ microflowers as high-rate and long-life cathodes for Mg-based hybrid-ion batteries†

Yanan Xu,^{‡a} Chang Xu,^{‡a} Qinyou An,^{*a} Qiulong Wei,^a Jinzhi Sheng,^a Fangyu Xiong,^a Cunyuan Pei^a and Liqiang Mai^{‡*ab}

Novel NASICON-type carbon-coated $\text{LiTi}_2(\text{PO}_4)_3$ microflowers (LTP-F/C) as a hybrid magnesium–lithium-ion battery (MLIB) cathode is presented for the first time. Benefiting from the synergistic effect of the NASICON structure, nanosheet-constructed hierarchical architecture, and uniform carbon coating of LTP-F/C, this hybrid MLIB exhibits extraordinary electrochemical performance: ultra-high cycling stability (capacity retention of 80% after 3000 cycles at 10 C) and outstanding rate capability (94 mA h g^{-1} at 20 C) under a high discharge voltage plateau of ~ 1.71 V (vs. Mg/Mg²⁺). This hybrid battery system design is highly promising for large-scale energy storage applications.

Introduction

Today, high-performance, low-cost and safe energy storage technology is still one of the biggest challenges faced by human society.^{1,2} Lithium-ion batteries (LIBs) have always been considered to be one of the promising candidates due to their high voltage and high energy density. However, the cost and safety issues of LIBs are detrimental for further application.^{3,4} Magnesium-ion batteries (MIBs) have gained considerable popularity as a promising electrochemical system owing to their

abundant resources and low cost.^{5–9} Benefiting from the two-electron nature of Mg²⁺, the MIBs deliver a theoretical volumetric capacity of 3833 mA h cm^{-3} , much higher than that of Li metal (2046 mA h cm^{-3}). Additionally, unlike many Li-ion and Na-ion anode materials, Mg anode can avoid the formation of solid-electrolyte interface (SEI) which causes irreversible capacity loss arising from the decomposition of the electrolyte at low anodic potentials.^{5,10} Most importantly, compared with lithium metal and sodium metal anodes, the Mg anode is dendrite-free during the deposition/dissolution process of Mg, suggesting higher security especially in the future practical application.^{8–11} These advantages make MIBs a promising candidate for an energy storage system with low cost and high-performance. However, the strong coulombic interaction between the electrode material and the Mg²⁺ results in the sluggish solid-state diffusion of Mg²⁺, leading to low Mg²⁺ intercalation efficiency, large potential polarization, and rapid capacity decay during the charge/discharge.^{12,13} Thus, discovering new suitable intercalation cathode materials is still a big bottleneck faced in this field. To date, only the Chevrel phase family Mo_6X_8 (X = S, Se or their combination) exhibits the required reversible intercalation properties and stability for practical use,⁵ but the low voltage (1.1 V vs. Mg/Mg²⁺) and low energy density (140 W h kg^{-1}) cannot meet the requirements of high energy storage technologies. The fact of lacking a suitable intercalation host with high voltage and high capacity significantly hinders the practical implementations of MIBs.

To meet the demands of intercalation kinetics in the cathode and to fully exert the advantages of the Mg anode, hybrid magnesium–lithium-ion batteries (MLIBs) have been demonstrated as one promising strategy.¹⁴ The energy storage system combining both the advantages of fast Li-intercalation cathode and high-capacity Mg anode exhibits satisfactory energy density, power density and cycling stability. The operating mechanism of one MLIB system is shown in Fig. 1a: the electrolytes are dual salt electrolytes containing both Mg²⁺ and Li⁺ ions (all-phenyl complex (APC) and LiCl dissolved in THF), the fast Li⁺ intercalation/deintercalation occurs at the cathode side,

^aState Key Laboratory of Advanced Technology for Materials Synthesis and Processing, International School of Materials Science and Engineering, Wuhan University of Technology, Wuhan 430070, Hubei, P. R. China. E-mail: anqinyou86@whut.edu.cn; mlq518@whut.edu.cn

^bDepartment of Chemistry, University of California, Berkeley, California 94720, USA

† Electronic supplementary information (ESI) available: XRD patterns of bare LTP; nitrogen adsorption–desorption isotherms of LTP-F precursor, LTP-F/C and bare LTP; EDS elemental mappings and the EDS spectrum of the residual carbon skeleton after etching the LTP from LTP-F/C; SEM images of the bare LTP; TGA curves of LTP-F/C; the contribution ratio of the plateau discharge capacity of LTP-F/C at different rates; discharge/charge curves of the LTP-F/C cathode in the LTP-F/C|Mg²⁺|Mg cell (1st cycle), LTP-F/C|Li⁺|Li cell (1st cycle), at 1 C (C = 140 mA h g^{-1}) and corresponding cycling performances; SEM images of the LTP-F/C electrode after 3000 cycles at 10 C; SEM images of the Mg anode before cycling and after 3000 cycles at 10 C. See DOI: 10.1039/c7ta03392c

‡ These authors contributed equally to this study.

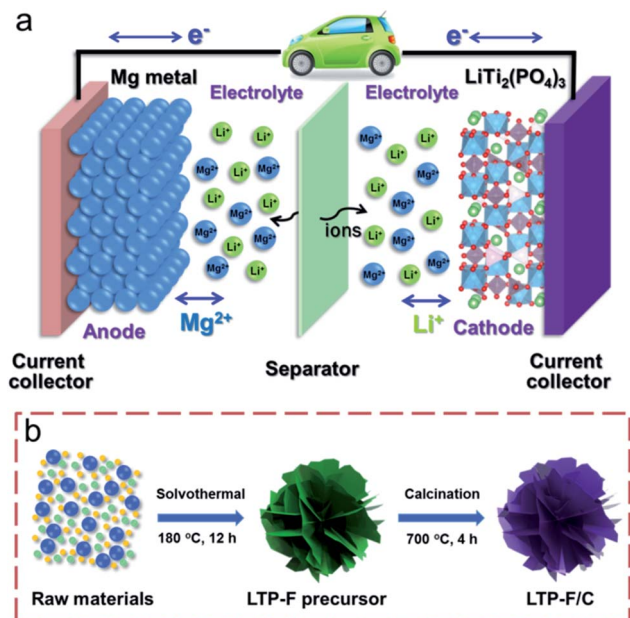


Fig. 1 Schematic illustrations of (a) the hybrid battery designed in this work and (b) the synthesis of LTP-F/C.

and the reversible Mg deposition/dissolution takes place at the anode side. But it is worth noting that the matching of the electrolyte and cathode is the key point when designing the MLIBs. For example, the APC electrolyte has a cut-off upper voltage of 3.0 V (*vs.* Mg/Mg²⁺), but it decreases to 2.5 V (*vs.* Mg/Mg²⁺) when LiBF₄ is added due to a side reaction.¹⁴ Besides, in order to avert the corrosion of normal non-inert metal current collectors (such as stainless steel) by an electrolyte, the upper voltage of the APC must be under 2.0 V (*vs.* Mg/Mg²⁺).¹⁵ Therefore, the operation potential of the chosen cathode should be limited inside the stability window of the hybrid electrolytes. Previous MLIB reports consist of a series of LIB cathodes such as TiS₂,^{10,16} Mo₆S₈,¹⁷ TiO₂,¹⁸ Li₄Ti₅O₁₂,^{9,19} MoS₂,²⁰ Ti₃C₂T_x,²¹ and even high-voltage LiFePO₄,²² Prussian blue,²³ and MgCo₂O₄,²⁴ which exhibit remarkable Li-insertion properties in the dual salt electrolyte systems. However, the output voltages or energy densities of the former cathodes are relatively low. The operation potentials of the latter are outside the stability window of the electrolyte for the rechargeable MIBs with a low-cost stainless steel current collector. These are disadvantageous for practical application. With these considerations, a much more effective cathode material with higher performance and excellent stability in the dual salt electrolyte is urgently needed. Recently, a sodium super-ionic conductor (NASICON) N_xM₂(PO₄)₃ (M = transition metal and N = Li or Na) structure has been developed as the electrode with promising electrochemical performance benefiting from a three-dimensional (3D) large open framework which allows rapid and reversible ion diffusion in the lattice.^{3,4,25–27} Among these, LiTi₂(PO₄)₃ (LTP) is a promising cathode for using in energy storage systems especially in aqueous LIBs.^{28–30} But for the Mg-based batteries, the relative high and safe insertion potential of 1.71 V (*vs.* Mg/Mg²⁺), fast ion diffusion ability and high theoretical energy

density (~240 W h kg⁻¹) of LTP endow significant advantages, which has not been reported before.

Herein, for the first time, we report a high-performance MLIB with NASICON-type LTP as the cathode, dendrite-free Mg metal as the anode, APC-LiCl as the electrolyte and low-cost stainless steel as the current collector. The APC-LiCl complex electrolyte offers highly reversible Mg deposition/dissolution, which has been demonstrated by previous studies.^{10,16} Stainless steel was chosen as the current collector in terms of the stability of the electrolyte (≤2 V) and low cost. The carbon-coated LiTi₂(PO₄)₃ microflowers (LTP-F/C) were synthesized by means of a facile solvothermal method and subsequent annealing treatment (Fig. 1b). In brief, tetrabutyl titanate (TBOT), LiH₂PO₄, H₃PO₄ and ascorbic acid are dissolved in a mixed solvent (ethylene glycol (EG) and deionized water) followed by a solvothermal treatment. Through self-assembling, LTP microflower precursors are obtained. After annealing in Ar atmosphere, this unique three dimensional (3D) structure is well duplicated. The experimental details are described in the Experimental section. The well designed hierarchical LTP-F/C provides a rapid ion-diffusion and charge-transfer kinetics resulting from the synergistic effect of the open NASICON crystal structure of LTP and 3D carbon framework. Meanwhile, the as-synthesized LTP-F/C is endowed with high structural stability, leading to excellent cycling performance. As a control experiment, the microflower precursor annealing in air atmosphere results in carbon-free LTP (denoted as bare LTP).

Experimental section

All chemicals were purchased from Aladdin or Sigma Aldrich and used as received without further purification.

Materials synthesis and characterization

The LTP-F/C was prepared by means of a facile solvothermal method and subsequent annealing treatment. First, 2 mmol TBOT was added into 10 mL of the ethylene glycol (EG) solvent. After vigorously stirring for 30 min a transparent solution was obtained. Then 0.1 M LiH₂PO₄, 2 mM H₃PO₄, and 0.1 M ascorbic acid were dissolved in 20 mL of deionized water and slowly added into the above solution. The transparent solution gradually turned to yellow and was further stirred for 1 h to obtain a homogenous and transparent solution. Then the above solution was transferred into a 50 mL Teflon-lined stainless steel autoclave and kept at 180 °C for 12 h, followed by natural cooling to room temperature. Then the precursor was dried at 70 °C and further dried at 120 °C. The collected brown powder product was ground, and then it was annealed at 350 °C for 2 h followed by annealing at 700 °C for 4 h in Ar at a heating rate of 2 °C min⁻¹ to finally obtain the LTP-F/C. As a control experiment, the bare LTP was prepared through the same process with LTP-F/C but annealed in air atmosphere to remove the carbon. XRD (Burker D8 Advanced X-ray diffractometer with Cu-K α radiation) was employed to obtain the crystallographic information of the two samples. CHNS elemental analysis and thermogravimetric analysis (TGA, STA-449C) were conducted in

determining the carbon content of the LTP-F/C. Brunauer–Emmett–Teller (BET) surface areas were measured using a Tristar II 3020 instrument by adsorption of nitrogen at 77 K. The SEM images were collected with a JEOL-7100F microscope. The TEM and HRTEM images were obtained by using a JEM-2100F STEM/EDS microscope.

Preparation of electrolytes

The all-phenyl complex (APC) electrolytes were prepared according to Oren Mizrahi *et al.*³¹ First, 0.667 g of aluminum chloride (Aldrich, 99.99%) was dissolved in 15 mL of THF (Aldrich, 99.9% and dried by activated 4 Å molecular sieves) under vigorous stirring and kept for at least 12 h. Then the transparent solution was added dropwise to phenyl magnesium chloride (Macklin, 2 M solution in THF) under continuous stirring for another 12 h to form the APC solution. For the hybrid cell, 1 M LiCl was added into the APC electrolyte.

Electrochemical characterization

The electrochemical properties were evaluated by assembly of 2016 coin cells in a glove box filled with pure argon gas. The active electrode was made by using a mixture of 80 wt% active material, 10 wt% carbon black, and 10 wt% polytetrafluoroethylene (PTFE) binder. Then the working electrode was dried in a vacuum oven for 6 h at 100 °C. The mass loading of each electrode is around 2.0 mg cm⁻². In magnesium full cells, the magnesium metal was used as the anode, APC + 1 M LiCl was used as the electrolyte, stainless steel was used as the current collector, and glass fiber was used as the separator. The galvanostatic charge–discharge tests were carried out at a voltage window of 0.5–2.0 V on a battery test system (LAND CT2001A). Cyclic voltammetry (CV) tests were performed at the electrochemical workstation CHI 600e. AC-impedance spectra were recorded using an Autolab PGSTAT 302N with an open-circuit voltage of 1.91 V and a sweep frequency of 0.01–100 000 Hz.

Results and discussion

The X-ray diffraction (XRD) patterns of the LTP-F/C and bare LTP are shown in Fig. 2a and S1,† respectively. All the diffraction peaks are well indexed to the NASICON structured LTP (JCPDS no. 00-035-0754),³² indicating high purity. The intense peaks suggest the highly crystalline characteristic of the two samples. The detailed morphology and structure of LTP-F/C were characterized by scanning electron microscopy (SEM) and transmission electron microscopy (TEM). Fig. 2b shows that the LTP-F precursors with a microflower-like morphology are composed of nanosheets with an average diameter of ~2 μm. The BET surface area of the LTP-F microflower precursors was measured to be 40.76 m² g⁻¹ (Fig. S2a†). After annealing in Ar atmosphere, this novel 3D hierarchical structure is well maintained (Fig. 2c). The BET surface area of LTP-F/C is 63.28 m² g⁻¹ (Fig. S2b†). The much higher surface area of LTP-F/C is due to the carbonization of organic species during the annealing process. The energy dispersive X-ray spectrum (EDS) elemental mappings exhibit the existence and uniform

distribution of Ti, P, and O in the LTP-F/C (Fig. 2d). The TEM images (Fig. 2e and f) prove that the intercrossed nanosheet assembly of the LTP-F/C composite, and the thickness of the nanosheets are within several nanometers. The high-resolution TEM (HRTEM) image (Fig. 2f inset) clearly displays lattice fringes with a *d*-spacing of 6.03 Å, corresponding to the (012) planes of the rhombohedral LTP. The thickness of the carbon layer is determined to be 3 nm. When the LTP/C-F is dipped in hydrofluoric acid to remove the LTP crystals, the carbon framework with a flower-like morphology is largely retained (Fig. S3†), demonstrating the uniform distribution of carbon on the surface of the LTP crystal. But for the bare LTP, without the protection of the carbon layer, the microflower structure is severely damaged during the high-temperature crystallization process (Fig. S4†). The SEM images show that the bare LTP sheets aggregate together to form an irregular block structure. The BET surface area of bare LTP is only 32.69 m² g⁻¹ (Fig. S2c†). Determined from CHNS elemental analysis, the carbon content of LTP-F/C is 5.8 wt%. The TGA curve also confirms the low carbon content as shown in Fig. S5.†

To investigate the electrochemical performances of the prepared samples, we assembled the full-cells (2016-type coin cell) with metallic magnesium as the anode, APC + 1 M LiCl as the electrolyte and stainless steel as the current collector. Fig. 3a shows the charge and discharge profiles of the LTP-F/C at 1 C (1 C = 140 mA g⁻¹) in 0.5–2.0 V. Such a hierarchically structured LTP-F/C electrode exhibits coupled flat charge and discharge plateaus at around 1.71 V (*vs.* Mg/Mg²⁺), corresponding to the redox pair of Ti³⁺/Ti⁴⁺, and offers a high lithium-ion intercalation capacity of 136 mA h g⁻¹ (based on the active mass of LTP), which is close to the theoretical capacity. After 400 cycles (Fig. 3b), the capacity retention of LTP-F/C is 94.0% with a high average coulombic efficiency of 99.96%. But for bare LTP (Fig. S6a and b†), there is no obvious voltage platform due to the extremely serious polarization, and the initial discharge capacity is only 21 mA h g⁻¹. Fig. 3c shows the rate performance of the LTP-F/C, where the rates range from 1 to 20 C. Obviously, compared with the bare LTP (Fig. S6c†), the LTP-F/C exhibits remarkable rate performance at different rates. At 1 C rate, the LTP-F/C delivers a high reversible capacity of 134 mA h g⁻¹. With the rate increased to 2, 5, and 10 C, the discharge capacity is as high as 132, 128, and 122 mA h g⁻¹, respectively. Even at the high rate of 20 C, a reversible discharge capacity of 94 mA h g⁻¹ is still achieved, corresponding to 70% of the capacity obtained at 1 C. When the rate is back to 10, 5, 2, and 1 C, the discharge capacity is almost the same as before, exhibiting outstanding reversibility. The corresponding discharge–charge curves of LTP-F/C at different rates are shown in Fig. 3d. Even at the high rate of 20 C, the voltage plateaus are still distinct. The contribution ratio of the plateau discharge capacity of LTP-F/C at different rates is shown in Fig. S6.† The result shows that each contribution ratio of the plateau discharge capacity occupies a large proportion, demonstrating high stability of the output voltage at different rates.

Moreover, the rate performances of LTP-F/C with the APC electrolyte involving other different amounts of LiCl (0.2, 0.4, 0.6, and 0.8 M) were performed to investigate the influence of

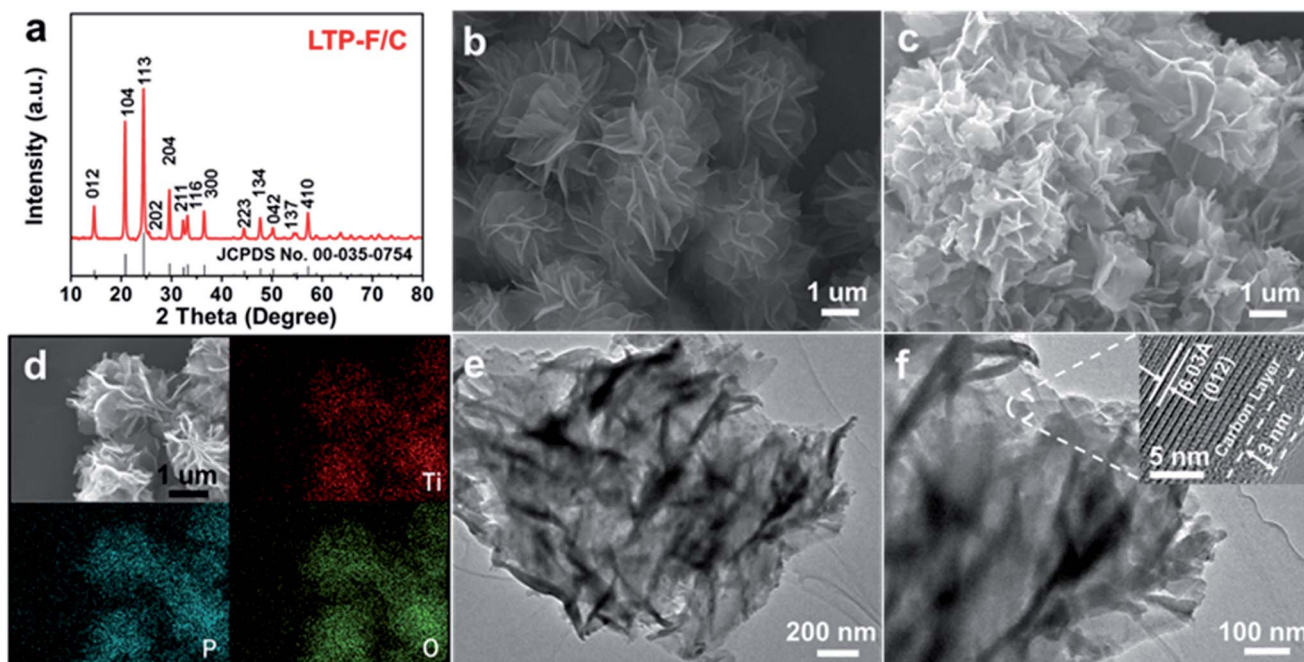


Fig. 2 (a) XRD pattern of LTP-F/C. (b) SEM image of LTP-F microflower precursors. (c) SEM image, (d) EDS elemental mappings, (e and f) TEM images and (f) HRTEM image (inset) of LTP-F/C.

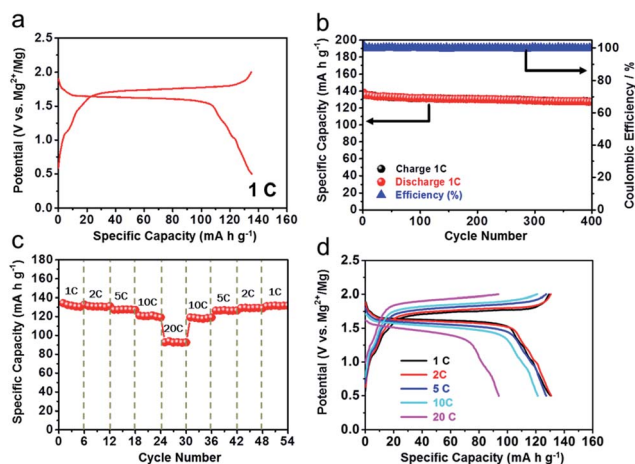


Fig. 3 Electrochemical properties of LTP-F/C with APC + 1 M LiCl as the electrolyte: (a) the initial discharge-charge curves and (b) cycling performances at 1 C. (c) The rate performances and (d) corresponding discharge-charge curves at different rates.

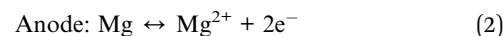
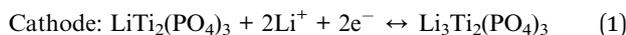
LiCl concentration on the electrochemical performance of the LTP-F/C (Fig. S8†). Obviously, with the increase of concentration of LiCl, the LTP-F/C exhibits better rate capability. Even though the raised viscosity results in low conductivity and has a negative effect on the electrochemical performance of the electrode, the effect of the increased Li^+ transference number counteracts the effect of low conductivity,^{33,34} so when the LiCl concentration is 1 M, the rate performance of LTP-F/C is obviously superior to that of other systems.

Fig. S9a† exhibits the cyclic voltammetry (CV) curves of LTP-F/C and bare LTP under a scan rate of 0.1 mV s^{-1} . Obviously, the well-designed LTP-F/C possesses a couple of redox peaks at around 1.82/1.55 V, matching well with the charge and discharge curves. But for the bare LTP, the redox peaks no longer exist due to the high overpotential. To reveal the reason for the enhanced electrochemical performance of LTP-F/C, electrochemical impedance spectra (EIS) measurements were carried out. The Nyquist plots are shown in Fig. S9b.† The charge transfer resistances (R_{ct}) of the two samples after two cycles are 486 and 1720Ω , respectively, indicating that the 3D hierarchical structure assembly of LTP-F/C provides more efficient electron/ion transport and the uniform dispersion of the 3D carbon skeleton on the surface of the LTP crystal largely improves the charge-transfer kinetics.

Two control experiments were also carried out to investigate the charge storage behavior of the hybrid MLIB. One is that the electrolyte is only APC without Li^+ , and the anode is magnesium metal, denoted as LTP-F/C| Mg^{2+} |Mg. Another is that the electrolyte is composed of THF and LiCl without Mg^{2+} , and the anode is lithium metal, denoted as LTP-F/C| Li^+ |Li. Fig. S10a† shows the charge and discharge profiles of the two different cells. In the LTP-F/C| Li^+ |Li system, the charge and discharge curves agree well with those of the hybrid Mg^{2+} / Li^+ battery (denoted as LTP-F/C| Mg^{2+} / Li^+ |Mg, Fig. 3a) apart from the different potentials. The plateau is at around 2.4 V (vs. Li/Li^+), which is identical to the previous reports applied in LIBs.^{35,36} During the charging and discharging process, the specific capacity is well maintained (Fig. S10b†). This demonstrates that the LiCl-THF electrolyte is comparable to the typical commercial LIB electrolyte that offers fast and high reversible Li^+

intercalation/deintercalation. But in the LTP-F/C|Mg²⁺|Mg cell, the LTP-F/C does not provide any capacity even after 100 cycles of activation, demonstrating that Mg²⁺ cannot insert into the LTP-F/C host in this system.

Moreover, to further investigate the structural evolution of LTP-F/C during lithium insertion and extraction, we performed the time-resolved *in situ* XRD and *ex situ* XRD techniques (Fig. 4). Fig. 4a shows the *in situ* XRD pattern tested in the LTP-F/C|Li⁺|Li systems. It can be observed that almost all the peak positions in the selective regions of LTP-F/C have no obvious change during the galvanostatic discharge and charge at the 1 C rate in the voltage window of 1.5–3.0 V. This may be due to the fact that the crystal structure of LTP-F/C is very stable, and in the lithium insertion and extraction process, due to the small size of lithium ions, the crystal structure of LTP-F/C has not changed, which shows the zero strain characteristics. Fig. 4b is the *ex situ* XRD pattern tested in the LTP-F/C|Mg²⁺|Li⁺|Mg systems at the 1 C rate in the voltage window of 0.5–2.0 V. Here, we perform the *ex situ* XRD instead of *in situ* XRD in the LTP-F/C|Mg²⁺|Li⁺|Mg systems due to the side reaction between the beryllium substrate and the electrolytes. The result shows that there is no peak disappearance and appearance in the selective reaction sites, which is well in accordance with the above *in situ* XRD result. This fully proves that the structural stability of the LTP-F/C and Mg²⁺ does not insert into LTP-F/C in the whole reaction process. Based on the above results, it is evident that the capacity contribution is completely determined by the Li⁺ intercalation/deintercalation in this hybrid battery system. In the discharge process, Li⁺ is intercalated into LiTi₂(PO₄)₃ at the cathode side and Mg is dissolved into the electrolyte from the Mg anode, while it is the inverse process during the charge process. The detailed reaction is given as follows:



To investigate the kinetics of ion solid-state diffusion, a galvanostatic intermittent titration technique (GITT) is performed as shown in Fig. S11.† The LTP-F/C delivers a specific capacity of 119 mA h g⁻¹ in the voltage window of 1.0–2.0 V, corresponding to a discharge product of Li_{1+x}Ti₂(PO₄)₃ (x = 1.74) (Fig. S11a†). In addition, based on the following formula, the Li-ion diffusion coefficient D^{GITT} (cm² s⁻¹) can be calculated from the potential response to a small constant current pulse (50 mA g⁻¹):³⁷

$$D^{\text{GITT}} = \frac{4}{\pi\tau} \left(\frac{m_{\text{B}} V_{\text{M}}}{M_{\text{B}} S} \right)^2 \left(\frac{\Delta E_{\text{s}}}{\Delta E_{\text{t}}} \right)^2 \quad (4)$$

where τ is the constant current pulse time, m_{B} , V_{M} , S , and M_{B} are the mass, molar volume, electrode–electrolyte interface area, and molar mass of LTP-F/C, respectively. ΔE_{s} is the voltage difference during the open-circuit period, and ΔE_{t} is the total change of the cell voltage during a constant current pulse excluding the IR drop (Fig. S11b†). Even the Li diffusivity decreases from 6.2×10^{-9} to 7.5×10^{-12} cm² s⁻¹ when the Li concentration increases in the host (Fig. S11c†) due to the charge repulsion, it evidently proves the fast charge-transfer kinetics and thus the enhanced rate capability.

The long cycling performance of LTP-F/C at a high rate of 10 C is shown in Fig. 5a. The initial discharge specific capacity is as high as 125 mA h g⁻¹ and a capacity retention of 80% after 3000 cycles. It is particularly worth mentioning here that the coulombic efficiency is almost 100% during the whole cycling process. The ultra-long cycling ability of LTP-F/C is very remarkable among the state-of-the-art reported hybrid MLIB

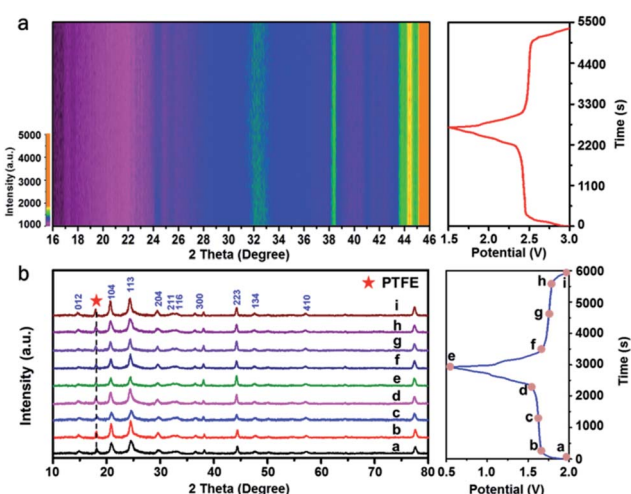


Fig. 4 (a) *In situ* XRD patterns of the LTP-F/C in LTP-F/C|Li⁺|Li systems during galvanostatic discharge and charge at 1 C and a voltage range of 1.5–3.0 V. (b) *Ex situ* XRD patterns of the LTP-F/C in LTP-F/C|Mg²⁺|Li⁺|Mg systems during the galvanostatic discharge and charge at 1 C and a voltage range of 0.5–2.0 V.

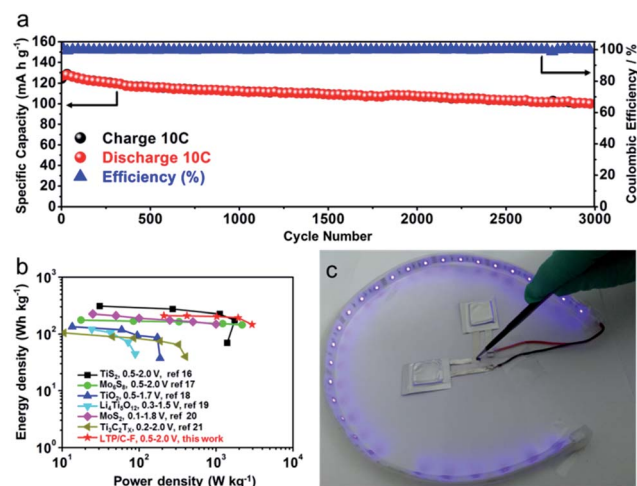


Fig. 5 (a) Long cycling performance of LTP-F/C at 10 C. (b) Comparison of the Ragone plots of LTP-F/C to the state-of-the-art electrodes of hybrid Mg²⁺/Li⁺ battery systems with a low-cost stainless steel current collector (≤ 2 V) (TiS₂,¹⁶ Mo₆S₈,¹⁷ TiO₂,¹⁸ Li₄Ti₅O₁₂,¹⁹ MoS₂,²⁰ and Ti₃C₂T_x (ref. 21)). (c) The lighted LED bulbs driven by the flexible pouch cell.

systems.^{10,16–24} Moreover, the SEM images of LTP-F/C after 3000 cycles at 10 C are shown in Fig. S12a and b.† Compared with the SEM images before cycling (Fig. 2c), the 3D hierarchical flower-like morphology is well maintained, indicating the excellent structural stability during Li⁺ insertion/extraction. The surface morphologies of the Mg anode before and after 3000 cycles at 10 C were also examined under SEM (Fig. S13a and b†), which display that no dendrites but irregular holes were formed.

Energy density and power density are important factors for characterizing the property of a secondary battery system for practical application.^{38,39} In particular, for MIBs, high energy and power density technologies are still the biggest challenges.⁸ Here, a comparison of the Ragone plots (energy density vs. power density) of the state-of-the-art electrodes of hybrid MLIB systems with a low-cost stainless steel current collector are displayed in Fig. 5b (all based on the cathode material). In terms of LTP-F/C, the energy density can be estimated to be 220 W h kg⁻¹ with a power density of 0.22 kW kg⁻¹. More significantly, the energy density still retains 147 W h kg⁻¹ with a power density of 2.94 kW kg⁻¹, which are amenable for practical applications compared with Mg-ion batteries based on Mo₆S₈ cathodes.⁵ Such an excellent result is significantly better than that of the current advanced cathodes among the hybrid MLIB systems, such as TiS₂,¹⁶ Mo₆S₈,¹⁷ TiO₂,¹⁸ Li₄Ti₅O₁₂,¹⁹ MoS₂,²⁰ and Ti₃C₂T_x.²¹ Flexible pouch cells were further fabricated to prove the viability of the well-designed LTP-F/C. It is clear that the obtained pouch-type battery is capable of lighting the LED bulbs (Fig. 5c). These results indicate that our hybrid battery system design is highly promising for practical energy storage applications.

Conclusions

In summary, a novel high-performance hybrid MLIB using NASICON-type hierarchical LTP-F/C microflowers as the cathode and dendrite-free Mg metal as the anode has been successfully fabricated. Combining the advantages of NASICON-type LTP and a 3D carbon skeleton, the unique 3D hierarchical structure offers rapid Li⁺ diffusion and electron transport, high electronic and ionic conductivity, and a stable structure during lithiation/delithiation, leading to outstanding high-rate capability (94 mA h g⁻¹ at 20 C) and ultra-long life cycling stability (capacity retention of 80% after 3000 cycles at 10 C with a high average coulombic efficiency of 99.99%). Moreover, this hybrid battery delivers an energy density up to 220 W h kg⁻¹ with a power density of 0.22 kW kg⁻¹, even when the power density is increased to 2.94 kW kg⁻¹, the energy density still retains 147 W h kg⁻¹, which is significantly better than that of Mg-ion batteries based on Mo₆S₈ cathodes and the state-of-the-art electrodes of hybrid MLIB systems with a low-cost stainless steel current collector. Our work demonstrates that the novel 3D hierarchical LTP-F/C is a highly promising cathode for MLIBs for commercial use.

Acknowledgements

This work was supported by the National Key Research and Development Program of China (2016YFA0202603), the National

Basic Research Program of China (2013CB934103), the Programme of Introducing Talents of Discipline to Universities (B17034), the National Natural Science Foundation of China (51521001, 51602239), the National Natural Science Fund for Distinguished Young Scholars (51425204), the Hubei Provincial Natural Science Foundation of China (2016CFB267), and the Fundamental Research Funds for the Central Universities (WUT: 2016III001, 2016III003, 2016IVA090, 2017III009, 2017III007). Prof. Liqiang Mai gratefully acknowledged the financial support from the China Scholarship Council (No. 201606955096).

Notes and references

- 1 B. Dunn, H. Kamath and J.-M. Tarascon, *Science*, 2011, **334**, 928–935.
- 2 S. Chu and A. Majumdar, *Nature*, 2012, **488**, 294–303.
- 3 Y. Xu, Q. Wei, C. Xu, Q. Li, Q. An, P. Zhang, J. Sheng, L. Zhou and L. Mai, *Adv. Energy Mater.*, 2016, **6**, 1600389.
- 4 C. Xu, Y. Xu, C. Tang, Q. Wei, J. Meng, L. Huang, L. Zhou, G. Zhang, L. He and L. Mai, *Nano Energy*, 2016, **28**, 224–231.
- 5 D. Aurbach, Z. Lu, A. Schechter, Y. Gofer, H. Gizbar, R. Turgeman, Y. Cohen, M. Moshkovich and E. Levi, *Nature*, 2000, **407**, 724–727.
- 6 C. B. Bucur, T. Gregory, A. G. Oliver and J. Muldoon, *J. Phys. Chem. Lett.*, 2015, **6**, 3578–3591.
- 7 P. Saha, M. K. Datta, O. I. Velikokhatnyi, A. Manivannan, D. Alman and P. N. Kumta, *Prog. Mater. Sci.*, 2014, **66**, 1–86.
- 8 H. D. Yoo, I. Shterenberg, Y. Gofer, G. Gershtinsky, N. Pour and D. Aurbach, *Energy Environ. Sci.*, 2013, **6**, 2265–2279.
- 9 N. Wu, Z. Yang, H. Yao, Y. Yin, L. Gu and Y. Guo, *Angew. Chem., Int. Ed.*, 2015, **127**, 5757.
- 10 T. Gao, F. Han, Y. Zhu, L. Suo, C. Luo, K. Xu and C. Wang, *Adv. Energy Mater.*, 2015, **5**, 1401507.
- 11 D.-M. Kim, Y. Kim, D. Arumugam, S. W. Woo, Y. N. Jo, M.-S. Park, Y.-J. Kim, N.-S. Choi and K. T. Lee, *ACS Appl. Mater. Interfaces*, 2016, **8**, 8554–8560.
- 12 J. Muldoon, C. B. Bucur and T. Gregory, *Chem. Rev.*, 2014, **114**, 11683–11720.
- 13 M. Walter, K. V. Kravchyk, M. Ibanez and M. V. Kovalenko, *Chem. Mater.*, 2015, **27**, 7452–7458.
- 14 S. Yagi, T. Ichitsubo, Y. Shirai, S. Yanai, T. Doi, K. Murase and E. Matsubara, *J. Mater. Chem. A*, 2014, **2**, 1144–1149.
- 15 S. Yagi, A. Tanaka, Y. Ichikawa, T. Ichitsubo and E. Matsubara, *J. Electrochem. Soc.*, 2013, **160**, C83–C88.
- 16 H. D. Yoo, Y. Liang, Y. Li and Y. Yao, *ACS Appl. Mater. Interfaces*, 2015, **7**, 7001–7007.
- 17 Y. Cheng, Y. Shao, J.-G. Zhang, V. L. Sprenkle, J. Liu and G. Li, *Chem. Commun.*, 2014, **50**, 9644–9646.
- 18 S. Su, Y. NuLi, Z. Huang, Q. Miao, J. Yang and J. Wang, *ACS Appl. Mater. Interfaces*, 2016, **8**, 7111–7117.
- 19 Q. Miao, Y. NuLi, N. Wang, J. Yang, J. Wang and S.-i. Hirano, *RSC Adv.*, 2016, **6**, 3231–3234.
- 20 C.-J. Hsu, C.-Y. Chou, C.-H. Yang, T.-C. Lee and J.-K. Chang, *Chem. Commun.*, 2016, **52**, 1701–1704.
- 21 A. Byeon, M.-Q. Zhao, C. E. Ren, J. Halim, S. Kota, P. Urbankowski, B. Anasori, M. W. Barsoum and Y. Gogotsi, *ACS Appl. Mater. Interfaces*, 2017, **9**, 4296–4300.

- 22 Y. Cheng, D. Choi, K. S. Han, K. T. Mueller, J.-G. Zhang, V. L. Sprenkle, J. Liu and G. Li, *Chem. Commun.*, 2016, **52**, 5379–5382.
- 23 X. Sun, V. Duffort and L. F. Nazar, *Adv. Sci.*, 2016, **3**, 1600044.
- 24 T. Ichitsubo, S. Okamoto, T. Kawaguchi, Y. Kumagai, F. Oba, S. Yagi, N. Goto, T. Doi and E. Matsubara, *J. Mater. Chem. A*, 2015, **3**, 10188–10194.
- 25 D. Sun, G. Jin, Y. Tang, R. Zhang, X. Xue, X. Huang, H. Chu and H. Wang, *J. Electrochem. Soc.*, 2016, **163**, A1388–A1393.
- 26 D. Kundu, E. Talaie, V. Duffort and L. F. Nazar, *Angew. Chem.*, 2015, **127**, 3495–3513.
- 27 E. Quartarone and P. Mustarelli, *Chem. Soc. Rev.*, 2011, **40**, 2525–2540.
- 28 D. Sun, X. Xue, Y. Tang, Y. Jing, B. Huang, Y. Ren, Y. Yao, H. Wang and G. Cao, *ACS Appl. Mater. Interfaces*, 2015, **7**, 28337–28345.
- 29 D. Sun, Y. Jiang, H. Wang, Y. Yao, G. Xu, K. He, S. Liu, Y. Tang, Y. Liu and X. Huang, *Sci. Rep.*, 2015, **5**, 10733.
- 30 D. Sun, Y. Tang, K. He, Y. Ren, S. Liu and H. Wang, *Sci. Rep.*, 2015, **5**, 17452.
- 31 O. Mizrahi, N. Amir, E. Pollak, O. Chusid, V. Marks, H. Gottlieb, L. Larush, E. Zinigrad and D. Aurbach, *J. Electrochem. Soc.*, 2008, **155**, A103–A109.
- 32 C. Mariappan, C. Galven, M.-P. Crosnier-Lopez, F. Le Berre and O. Bohnke, *J. Solid State Chem.*, 2006, **179**, 450–456.
- 33 L. Suo, Y.-S. Hu, H. Li, M. Armand and L. Chen, *Nat. Commun.*, 2013, **4**, 1481.
- 34 Y. Yamada, K. Furukawa, K. Sodeyama, K. Kikuchi, M. Yaegashi, Y. Tateyama and A. Yamada, *J. Am. Chem. Soc.*, 2014, **136**, 5039–5046.
- 35 J.-Y. Luo, L.-J. Chen, Y.-J. Zhao, P. He and Y.-Y. Xia, *J. Power Sources*, 2009, **194**, 1075–1080.
- 36 V. Aravindan, M. Ulaganathan, W. C. Ling and S. Madhavi, *ChemElectroChem*, 2015, **2**, 231–235.
- 37 Q. An, Y. Li, H. D. Yoo, S. Chen, Q. Ru, L. Mai and Y. Yao, *Nano Energy*, 2015, **18**, 265–272.
- 38 H. Lai, Q. Wu, J. Zhao, L. Shang, H. Li, R. Che, Z. Lyu, J. Xiong, L. Yang and X. Wang, *Energy Environ. Sci.*, 2016, **9**, 2053–2060.
- 39 T. Zhang, J. T. Li, J. Liu, Y. P. Deng, Z. G. Wu, Z. W. Yin, J. H. Wu, L. Huang and S. G. Sun, *ChemElectroChem*, 2016, **3**, 98–104.